

Establishing the Magnetoelastic Origin of Spin-Wave Routing through Focused Ion Beam Patterning

Felix Naunheimer^{*1}, Johannes Greil¹, Valentin Ahrens¹, Levente Maucha², Ádám Papp², György Csaba², and Markus Becherer¹

¹TUM School of Computation, Information and Technology, Technical University of Munich, Munich, Germany

²Faculty of Information Technology and Bionics, Pázmány Péter Catholic University, Budapest, Hungary

February 12, 2026

Abstract

Spin waves are promising information carriers for analog and wave-based computing, requiring compact and precisely engineered scattering landscapes. Focused ion beam (FIB) irradiation enables such control by locally modifying the spin-wave dispersion in yttrium iron garnet (YIG), yet the underlying crystallographic mechanisms remain unclear. Here, we present an experimentally validated framework that attributes FIB-induced spin-wave steering to magnetoelastic effects arising from irradiation-induced lattice dislocations. Following FIB irradiation and wet-chemical etching, local height profiles were obtained by atomic force microscopy (AFM) and used as fixed geometric constraints in fits of spin-wave dispersion relations measured by time-resolved magneto-optical Kerr effect (trMOKE) microscopy. The dispersion relation was extended by an explicit magnetoelastic field term, treated as a fit parameter. Its evolution reveals three successive deformation regimes, elastic, plastic, and partial amorphization, explaining the observed non-monotonic dependence of the spin-wave wavelength on ion dose. A three-phase deformation scenario based on SRIM simulations reproduces the extracted magnetoelastic field trends, validating the fitting approach. Micromagnetic simulations incorporating strain tensors derived from the experimental magnetoelastic field reproduce the characteristic non-monotonic wavelength behavior. These results establish a physical basis for FIB-engineered graded-index (GRIN) spin-wave landscapes and magnetoelastically programmable magnonic devices.

1 Introduction

Analog computing is attracting renewed attention in the era of AI, particularly in application domains where CMOS technology encounters fundamental limitations. Rather than aiming to replace CMOS in general-purpose digital logic, alternative wave-based approaches focus on specialized, high-frequency, low-power, and non-Boolean computing tasks [1].

In this context, spin waves, collective excitations of a spin system that propagate precessional motion in a wave-like manner, are emerging as promising information carriers. Their quasiparticles, called magnons, naturally allow for operation in the gigahertz regime [2], making them intrinsically suited for microwave and RF signal-processing applications where low-power CMOS implementations remain challenging. Moreover, their wavelengths at gigahertz frequencies can be orders of magnitude shorter than those of electromagnetic waves, reaching

^{*}felix.naunheimer@tum.de

the sub-micrometer scale. This wavelength compression enables highly compact analog processing elements and interference-based computing structures that cannot be efficiently realized with conventional RF electronics [1, 2].

Crucially, many spin-wave functionalities are governed by the local dispersion relation: for a fixed excitation frequency, a controlled local change in the dispersion translates into a controlled change of the local wave vector and wavelength. Despite their nonlinear dispersion, spin waves admit close analogies to optics and support quasi-optical elements [3]. Spatially tailoring the effective magnetization, and thus the local spin-wave dispersion, allows the realization of graded refractive-index (GRIN) profiles for precise routing of spin waves [4]. In magnonic implementations, the term “GRIN” therefore refers to an engineered spatial profile of the dispersion (or equivalently the local wavelength at a given frequency), which governs the bending of wave fronts and the focusing or defocusing of spin-waves. Such quasi-optical elements include lenses and related routing geometries [5]. More complex scattering landscapes, e.g., those obtained by inverse design, have also been explored, but they ultimately rely on the same physical requirement: a reproducible, quantitative handle on how local magnetic modifications translate into local dispersion engineering [6, 7].

Among available nanofabrication approaches, focused ion beam (FIB) irradiation provides an attractive route to implement such dispersion landscapes in yttrium iron garnet (YIG), owing to its high spatial resolution and the tunability of the interaction depth via acceleration voltage and ion species. Ion-based magnetic modification has been used in several magnetic-device contexts, including field-coupled magnetic logic [8, 9] and the controlled nucleation and motion of skyrmions [10, 11]. In YIG specifically, localized ion implantation has been shown to enable dispersion-tunable, low-loss spin-wave waveguides [12]. In the context of spin-wave routing, our group previously demonstrated that 30 keV Ga^+ FIB irradiation can locally modulate the effective magnetization and thereby steer spin-wave wavefronts [5, 13, 14].

Despite these device-level demonstrations, the crystallographic and microstructural origin of FIB-induced dispersion shifts in YIG thin films remains insufficiently established. Earlier interpretations, captured wavelength changes using an effective, phenomenological strain-induced anisotropy. While light-ion implantation is indeed known to increase strain-induced anisotropy in garnet films [15], such approximations do not fully explain key experimental trends, in particular the non-monotonic (approximately parabolic) evolution of the effective refractive-index-like response reported in [5, 14]. This motivates a model that explicitly accounts for irradiation-driven structural evolution, including defect generation, strain redistribution, and partial amorphization [16, 17].

In this work, we propose a three-phase scenario describing the structural evolution of ion-implanted YIG:

- (I) Strain accumulation driven by lattice dislocations formed in radiation-induced collision cascades;
- (II) Strain relaxation through the migration of dislocations toward regions of lower strain; and
- (III) Near-surface amorphization, accompanied by continued strain accumulation in deeper layers governed by the mechanisms active in phases (I) and (II).

We test this scenario using a self-consistent experimental–computational pipeline. Following focused-ion-beam (FIB) irradiation, wet-chemical etching is employed to remove the near-surface amorphous material formed in phase (III). The resulting local thickness reduction is quantified by atomic force microscopy (AFM) and used as a fixed geometric constraint in the subsequent analysis. Spin-wave dispersion relations are then measured in the etched regions using time-resolved magneto-optical Kerr effect (trMOKE) microscopy and analyzed by fitting the Kalinikos–Slavin formalism [18], extended by an explicit magnetoelastic field term to account for strain accumulation and relaxation associated with phases (I) and (II).

To justify the use of the magnetoelastic field as a representative parameter for irradiation-induced strain accumulation and relaxation, and the use of the local thickness reduction as an indicator of partial amorphization, we introduce an analogous three-phase scenario based on SRIM Monte Carlo simulations [19]. As a final consistency check, strain tensor components derived independently from the fitted magnetoelastic field and from the modeled strain evolution are implemented in micromagnetic simulations [20] to reproduce the experimentally observed trends in the dispersion of FIB-steered spin waves.

2 Methods

To investigate the impact of Ga^+ ion irradiation on propagating spin waves, the experimental setup shown schematically in Fig. 1 (not to scale) was employed.

A YIG thin film with a thickness of $t = 100$ nm was deposited by RF sputtering onto a 500 μm GGG substrate and subsequently annealed in an oxidation furnace to obtain the desired crystalline structure. For spin-wave excitation, a Ti(10 nm)/Au(100 nm) microstrip line (MSL) with a width of 2 μm was deposited by e-beam evaporation. Adjacent to the MSL, squares of $50 \times 50 \mu\text{m}^2$ were irradiated by direct FIB writing at varying Ga^+ ion doses ranging from 2 to 60×10^{12} ions/ cm^2 in steps of 2×10^{12} ions/ cm^2 . The irradiated regions were written at acceleration voltages of 30 keV, 16 keV, and 8 keV to obtain different penetration depths of the ions. To experimentally verify the reduction in effective film thickness caused by partial surface amorphization, as reported in [16], we introduced an additional wet-chemical etching step. The film was etched for 120 s, and the resulting stepwise changes in etching depth across the irradiated regions were quantified by atomic force microscopy (AFM).

Spin-wave propagation in the irradiated regions was investigated in the forward-volume spin-wave (FVSW) configuration. Spin waves were excited at a wavenumber k_0 in the unirradiated region beneath the stripline and coupled into the irradiated area, where the wavenumber changed to k_{FIB} , as illustrated in Fig. 1. Upon exiting the irradiated square, the wavenumber reverted to its original value k_0 . The experiment was conducted using trMOKE microscopy, allowing us to analyze spin-wave propagation across 30 distinct implantation regions as well as in the pristine film at the intrinsic wavenumber k_0 . This approach enabled us to track the evolution of the spin-wave dispersion as a function of implantation dose and to extract key parameters through fits to the Kalinikos–Slavin model. The measurements were carried out at spin-wave excitation frequencies between 2.285 GHz and 2.33 GHz in steps of 5 MHz, using an input power of 8 dBm with an applied external magnetic field of $\mu_0 H_{\text{ext,OOP}} = 250$ mT in the out-of-plane (OOP) direction.

To model the depth-dependent damage profile induced by Ga^+ ion irradiation, SRIM Monte Carlo simulations were performed. The simulations calculate the energy loss of individual ions within the crystal lattice and generate displacement cascades that lead to the formation of vacancies, interstitials, and lattice disorder throughout the film thickness.

The ion species was defined as Ga^+ with a mass of approximately 70 u. Acceleration voltages of 30 keV, 16 keV, and 8 keV were used to study the energy dependence of the damage profile. The simulated YIG layer had a density of 5.17 g/ cm^3 and a thickness of 100 nm, with a stoichiometry of $\text{Y}_3\text{Fe}_5\text{O}_{12}$. Displacement energies of $E_{\text{Y}} = 66$ eV, $E_{\text{Fe}} = 56$ eV, and $E_{\text{O}} = 40$ eV were used [21]. To minimize channeling effects [16], the ion beam was tilted by 7° with respect to the surface normal.

From the SRIM output, the depth-dependent damage profile expressed in units of $(\text{atoms}/\text{cm}^3)/(\text{ions}/\text{cm}^2)$, is given. By multiplying this profile with the experimentally applied ion dose, the depth-dependent damage model DM_{FIB} was constructed, yielding the local damage density as a function of depth in units of atoms/cm^3 .

Micromagnetic simulations were performed to justify the magnetoelastic origin of the experimentally observed dispersion shifts. A magnetoelastic coupling constant of $B_1 = 3.48 \times 10^5$ J/ m^3

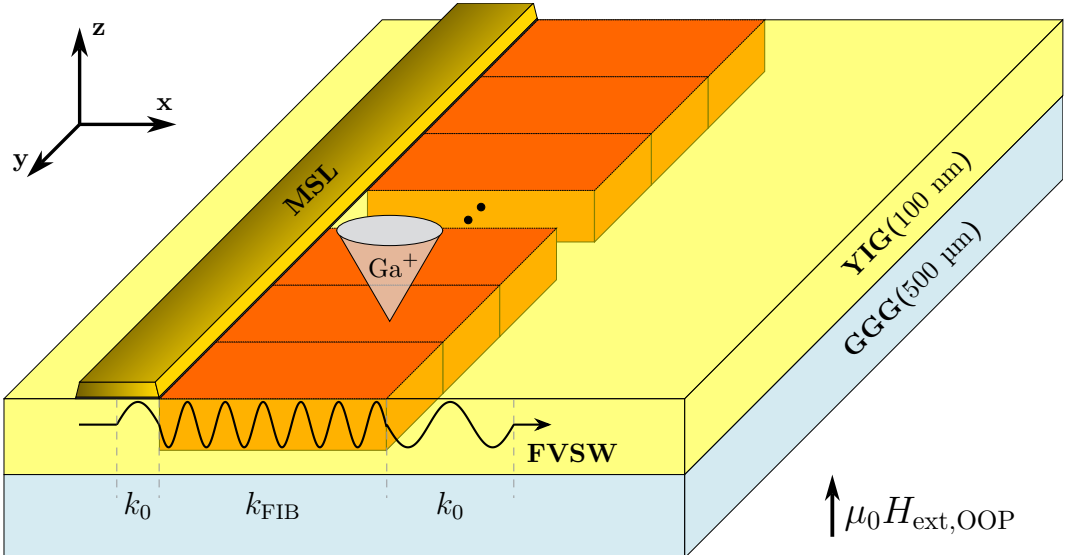


Figure 1: Schematic overview of a 100 nm YIG thin film deposited by RF-Sputtering on a 500 μm GGG substrate. Spin wave excitation is provided by a 2 μm wide, 110 nm thick Ti(10 nm)/Au(100 nm) MSL. Adjacent to the antenna, squares of $50 \times 50 \mu\text{m}^2$ (red), were irradiated with Ga^+ ion doses ranging from 2 to $60 \times 10^{12} \text{ ions/cm}^2$ in steps of $2 \times 10^{12} \text{ ions/cm}^2$. In the FVSW configuration, spin waves are excited at a k_0 wave vector directly beneath the antenna. Upon entering the irradiated regions, the wave vector changes to k_{FIB} , and returns to k_0 after leaving the region.

was used for YIG [22], together with a Poisson ratio of $\nu = 0.29$ [23]. The saturation magnetization was set to $M_s = 130 \text{ kA/m}$, as determined from on-chip ferromagnetic resonance (FMR) measurements.

3 Results

3.1 Spin-Wave Scattering in Ion-Implanted Thin Films

As previously demonstrated by our group [5], Ga^+ ion irradiation via direct FIB writing on a YIG thin film modifies the magnetic properties and, consequently, the spin-wave wavelength. To correlate the wavelength modification with the corresponding ion dose, we constructed a characteristic dosemap comprising 30 irradiation regions, as shown in Fig. 2. The dosemap captures the spin-wave scattering across regions implanted at an ion acceleration of 30 keV, with doses ranging from $2\text{--}60 \times 10^{12} \text{ ions/cm}^2$. The plane-wave fronts measured by trMOKE at 2.305 GHz and 8 dBm input power with $\mu_0 H_{\text{ext,OOP}} = 250 \text{ mT}$ (Fig. 2(a)) were analyzed via a line-wise Fourier transformation along the x -direction to extract the carrier wavelength λ (Fig. 2(b)). This analysis reveals two clear turning points at doses of $12 \times 10^{12} \text{ ions/cm}^2$ and $34 \times 10^{12} \text{ ions/cm}^2$, which divide the dose-dependent response into three monotonic wavelength regimes. These regimes are characterized by decreasing (I), increasing (II), and again decreasing (III) wavelengths.

In Ref. [5], wavelength regimes I and II were attributed to strain-induced magnetic anisotropy generated by ion irradiation, which modifies the effective magnetization M_{eff} and thereby shifts the spin-wave dispersion to shorter or longer wavelengths. While this strain-induced anisotropy captures monotonic trends of the wavelength evolution, it does not account for the pronounced turning points that define the three regimes in Fig. 2(b). As we show in the following sections, these features arise from the nucleation and motion of irradiation-induced crystalline dislocations within the YIG lattice, which establish the strain responsible for the observed anisotropy.

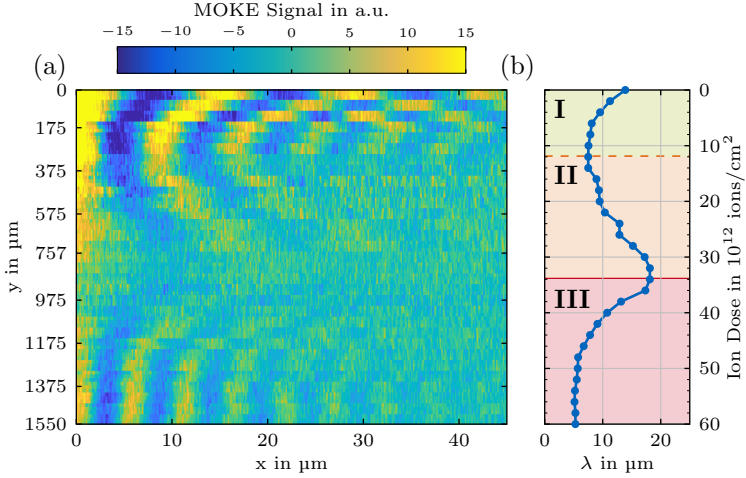


Figure 2: trMOKE measurement of a $t = 100$ nm wet-chemically etched YIG film at 2.305 GHz and 8 dBm input power with $\mu_0 H_{\text{ext,OOP}} = 250$ mT. (a) trMOKE image of coherently excited spin waves across 30 distinct Ga^+ -implanted regions (irradiated at 30 keV) over a propagation distance of 45 μm . (b) Line-wise Fourier transformations of the spin-wave profiles in (a) reveal wavelength shifts as a function of ion dose. Three prominent wavelength regimens are observed: I between the unimplanted reference (0×10^{12} ions/ cm^2) and the first turning point at 12×10^{12} ions/ cm^2 ; II between 12×10^{12} ions/ cm^2 and 34×10^{12} ions/ cm^2 ; and III extending from 34×10^{12} ions/ cm^2 to a saturation regime near 60×10^{12} ions/ cm^2 .

3.2 Three-Phase Scenario for Irradiation-Induced Deformations

To evaluate the stability and mechanical strength of a material, stress testing is commonly employed to characterize its stress-strain response. The characteristic stress response of a material under linearly increasing strain is represented by its stress-strain curve (Fig. 3). This curve illustrates the transition from the reversible elastic deformation regime to the irreversible plastic deformation regime, ultimately culminating in a destructive deformation regime of the specimen.

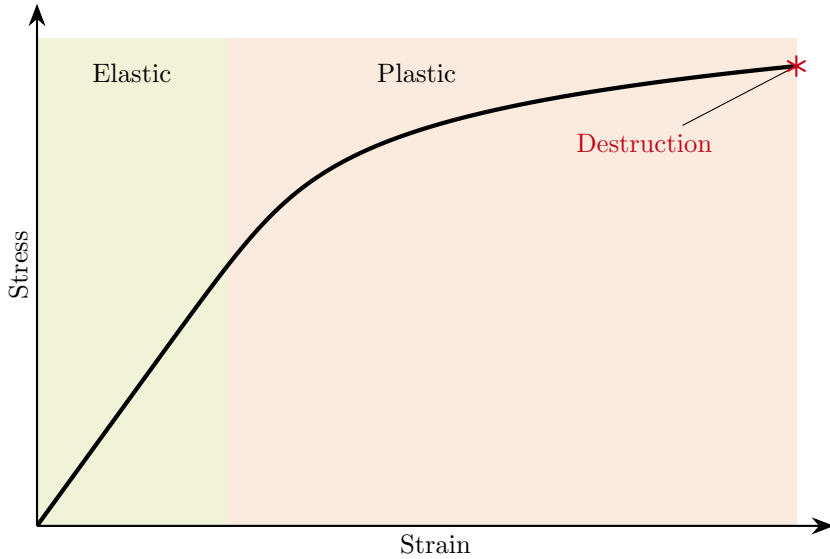


Figure 3: Schematic stress-strain curve of a crystal under continuous irradiation, illustrating elastic and plastic deformation up to the breakdown of the crystalline structure.

As these regimes originate at the atomic scale, the concept of a stress-strain curve can be extended to describe the effects of ion irradiation on crystalline materials. In this analogy, ion irradiation acts as an effective pressure applied to the lattice, gradually altering its internal structure. When accelerated ions penetrate the crystal, they initiate collision cascades that displace atoms from their lattice sites, producing a vacancy-rich core surrounded by an interstitial atom shell. With increasing irradiation dose, these defect regions grow and aggregate into compact clusters (Fig. 4(a)). These clusters subsequently collapse into energetically favored edge dislocation (\perp) loops, as shown in Fig. 4(b), which bend the surrounding lattice and induce strain [17]. Figures 4(c)-4(d) illustrate the lattice bending produced by these dislocation loops. A vacancy-type loop generates an edge dislocation with step-like distortions in the adjacent lattice planes (Fig. 4(c)), while Fig. 4(d) shows the corresponding structure formed by an interstitial loop. As the irradiation dose increases, the density of such loops grows accordingly, which increases the magnitude of induced strain.

With the strain mechanism established, we turn to the stress-strain curve a crystalline material undergoes when exposed to ion irradiation, as illustrated in Fig. 3. To describe this curve, we map the elastic, plastic, and destructive deformation regimes onto three phases within a strain-potential landscape. This landscape is developed by orienting the description around the Peierls potential, which represents the periodic lattice energy barrier that must be overcome for a dislocation to move to an adjacent lattice row [24]. The description further builds on established understanding of dislocation formation and nucleation under ion irradiation [17]. This strain-potential landscape can be viewed as a simplified, one-dimensional representation of the crystal lattice (Fig. 5). In this picture, the lattice is modeled as a sequence of potential wells distributed along the material depth, each separated by a barrier analogous to the Peierls

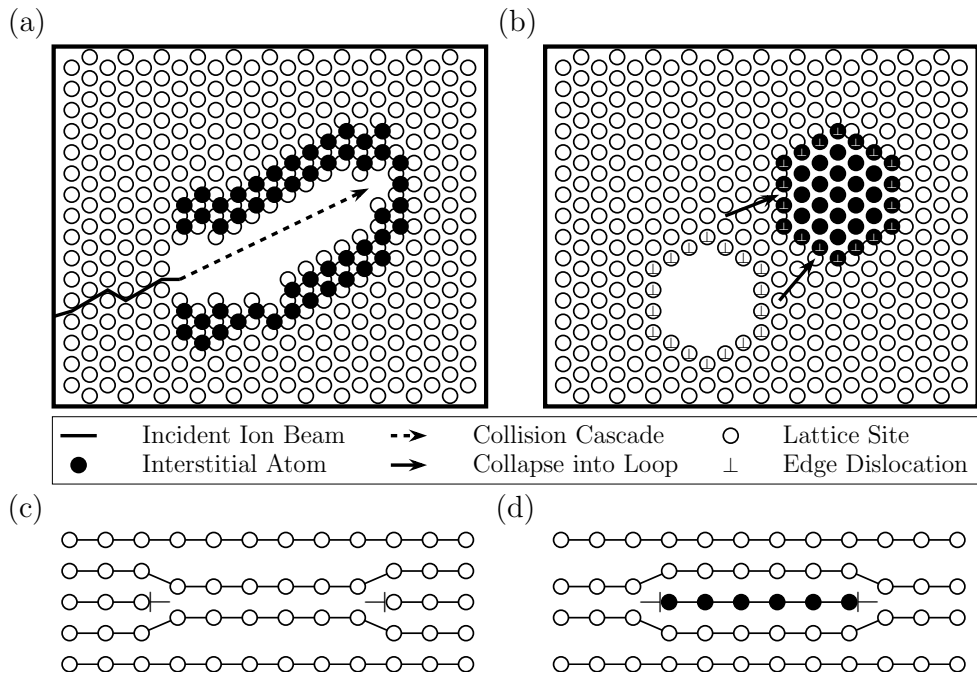


Figure 4: Illustration of the dislocation formation. (a) An incident ion beam initiates collision cascades that displace atoms from their lattice sites, creating a vacancy-rich core surrounded by interstitial atoms that aggregate into a defect cluster. (b) With increasing defect concentration, the cluster collapses into an energetically favored edge dislocation (\perp) loop. (c) A vacancy-type dislocation loop corresponds to a missing atomic plane, causing the surrounding lattice to bend inward toward the vacant lattice sites. (d) An interstitial-type dislocation loop corresponds to an additional atomic plane, pushing the lattice outward from the additional plane.

potential. These barriers represent the strain that must be overcome for a dislocation to move from one lattice row to the next.

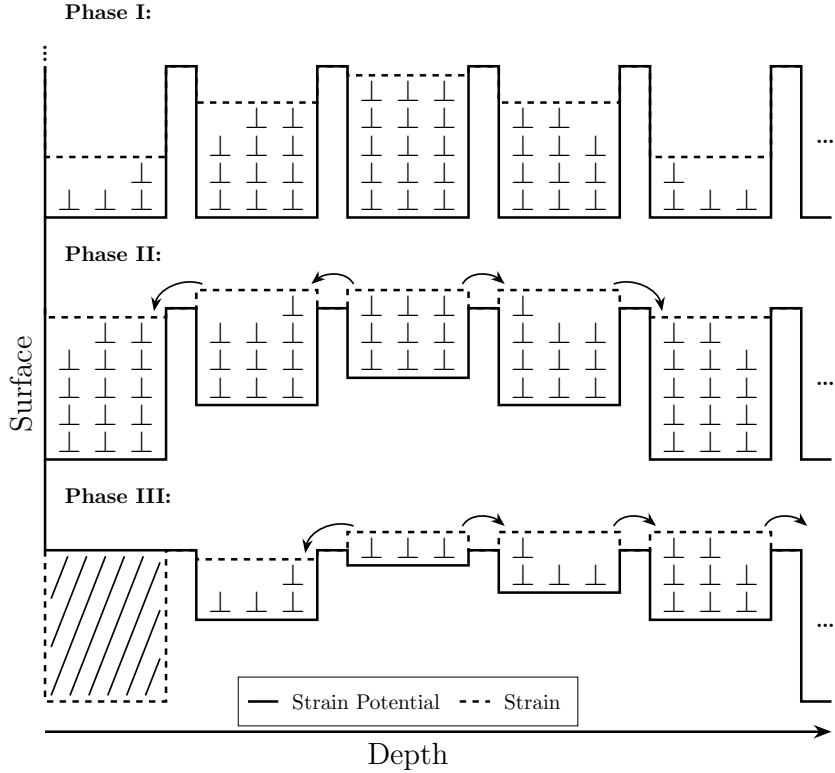


Figure 5: Conceptual illustration of strain potential wells that translate dislocation dynamics into a three-phase scenario of irradiation-induced deformations. Phase I: Dislocations (\perp) nucleate and accumulate within the strain well at the ion-damage source, progressively filling it in a process known as source hardening. Phase II: As the local strain exceeds the potential threshold, dislocations overcome the barrier and migrate into neighboring wells, initiating plastic deformation. Phase III: Migrated dislocations pile up against obstacles such as surfaces, defects, or grain boundaries, producing friction hardening and ultimately leading to partial amorphization (//).

In the following, we define a three-phase deformation scenario that captures the evolution of dislocation behavior and strain accumulation under increasing ion irradiation. In phase I, dislocations nucleate and begin to pile up around the ion-induced damage region. As the ion dose increases linearly, the number of dislocations rises proportionally, and the accumulated strain increases in a nearly linear manner, characteristic of an elastic response. In the strain-potential landscape, this corresponds to the potential well at the damage source gradually filling with dislocations, which is known as source hardening. In phase II, the increasing strain becomes sufficient for dislocations to overcome the potential barriers between neighboring wells. Once this threshold is exceeded, dislocations begin to move, interact, and rearrange, marking the onset of plastic deformation. In Fig. 5, this corresponds to dislocations hopping from one well to the next as the local stress surpasses the Peierls-like barrier. Importantly, dislocations preferentially migrate toward regions of lower strain, thereby partially relaxing the local strain while redistributing deformation throughout the lattice. In phase III, the migrated dislocations accumulate once more, but now they pile up against obstacles such as the material surface, defects, or grain boundaries, which is known as friction hardening. Unlike in phase II, the locally increasing strain is no longer sufficient to overcome the potential barriers at these obstacles. As a result, dislocations become trapped, leading to a buildup of strain that cannot be relieved by further migration. In the strain-potential landscape, this corresponds to an effectively infinite

barrier at the obstacle, producing a completely filled potential well that represents the maximum local strain the lattice can sustain. When this limit is reached, the crystalline order begins to break down, marking the onset of partial amorphization.

3.3 Spin-Wave Dispersion in the Presence of Magnetoelastic Fields and Local Thickness Reduction

To quantitatively link the three-phase scenario described above to the experimentally observed wavelength evolution in Sec. 3.1, we describe the effect of strain on spin-wave dynamics within the Landau–Lifshitz–Gilbert (LLG) formalism. The purpose of this section is to establish a direct correspondence between irradiation-driven strain evolution, experimentally accessible dispersion parameters, and the effective magnetic fields governing spin-wave propagation.

The strain state of a crystalline material is generally represented by the strain tensor

$$\boldsymbol{\varepsilon} = \begin{bmatrix} \varepsilon_{xx} & \varepsilon_{xy} & \varepsilon_{xz} \\ \varepsilon_{yx} & \varepsilon_{yy} & \varepsilon_{yz} \\ \varepsilon_{zx} & \varepsilon_{zy} & \varepsilon_{zz} \end{bmatrix}, \quad (1)$$

which captures both normal ($\varepsilon_{xx}, \varepsilon_{yy}, \varepsilon_{zz}$) and shear deformation components ($\varepsilon_{yx}, \varepsilon_{zx}, \varepsilon_{zy}$). In micromagnetic simulations, strain enters the spin dynamics through magnetoelastic coupling, giving rise to an additional effective field contribution \mathbf{H}_{mel} [25]. Within the LLG equation, the magnetization dynamics are governed by the total effective field

$$\mathbf{H}_{\text{eff}} = \mathbf{H}_{\text{eff},0} + \mathbf{H}_{\text{mel}}, \quad (2)$$

where the magnetoelastic contribution \mathbf{H}_{mel} directly couples lattice deformations to the magnetic precession, in addition to the strain-free field components contained in $\mathbf{H}_{\text{eff},0}$. The magnetoelastic contribution, \mathbf{H}_{mel} , can be expressed by Eq. (3), which is commonly used in micromagnetic simulations [25]

$$\mathbf{H}_{\text{mel}} = -\frac{2}{\mu_0 M_s} \begin{bmatrix} B_1 \varepsilon_{xx} m_x + B_2 (\varepsilon_{xy} m_y + \varepsilon_{zx} m_z) \\ B_1 \varepsilon_{yy} m_y + B_2 (\varepsilon_{xy} m_x + \varepsilon_{yz} m_z) \\ B_1 \varepsilon_{zz} m_z + B_2 (\varepsilon_{zx} m_x + \varepsilon_{yz} m_y) \end{bmatrix}, \quad (3)$$

where M_s is the saturation magnetization and B_1 and B_2 are the first and second magnetoelastic coupling constants, respectively. The vector $\vec{m} = (m_x, m_y, m_z)$ represents the normalized magnetization and is directly coupled to the corresponding strain tensor components given in Eq. (1). From the LLG equation, the spin-wave propagation characteristics can be described by the dispersion relation developed by Kalinikos and Slavin [18]

$$\omega = \sqrt{(\omega_0 + \omega_M \lambda_{\text{ex}} k^2)(\omega_0 + \omega_M \lambda_{\text{ex}} k^2 + \omega_M F)}, \quad (4)$$

with

$$F = P + \sin^2(\theta) \left(1 - P (1 + \cos^2(\phi)) \right. \\ \left. + \frac{\omega_M P (1 - P) \sin^2(\phi)}{\omega_0 + \omega_M \lambda_{\text{ex}} k^2} \right) \quad (5)$$

and

$$P = 1 - \frac{1 - e^{-tk}}{tk}. \quad (6)$$

Here, $\omega_0 = \gamma \mu_0 H_{\text{eff}}$ and $\omega_M = \gamma \mu_0 M_{\text{eff}}$ represent the scalar components in the spherical coordinate system defined by θ and ϕ , where γ is the gyromagnetic ratio and μ_0 the vacuum permeability. The parameter λ_{ex} denotes the exchange constant, and t is the thickness of the

magnetic film. The spin-wave wavenumber is given by $k = 2\pi/\lambda$, where λ is the spin-wave wavelength.

For the FVSW configuration, Eq. (5) simplifies to Eq. (6), since the in-plane component vanishes under perfect OOP magnetization ($\theta = 0^\circ$). Accordingly, Eq. (4) reduces to

$$\omega = \sqrt{(\omega_0 + \omega_M \lambda_{\text{ex}} k^2)(\omega_0 + \omega_M \lambda_{\text{ex}} k^2 + \omega_M P)}. \quad (7)$$

Within this formalism, the effects of elastic and plastic deformation, as well as partial amorphization, on spin-wave propagation can be described through Eq. (7). The magnetic strain response is captured by ω_0 . It reflects the accumulation and relaxation of strain through variations in Eq. (3) relative to Eq. (1), and consequently in the effective field H_{eff} as defined in Eq. (2), arising from dislocation accumulation and migration. In contrast, the effects of partial amorphization are accounted for by defining an effective magnetic film thickness, $t = t_{\text{eff}}$, which enters Eq. (7) through Eq. (6).

Accordingly, M_{eff} and $H_{\text{eff},0}$ are used as fitting parameters only once, by fitting Eq. (7) to the dispersion of the pristine film ($H_{\text{mel}} = 0$) shown in Fig. 6 (dark green markers). The resulting values are then fixed, and subsequent fits to the dispersion in the irradiated regions are used exclusively to extract the dose-dependent variations of $H_{\text{mel}} \neq 0$ in Eq. (2).

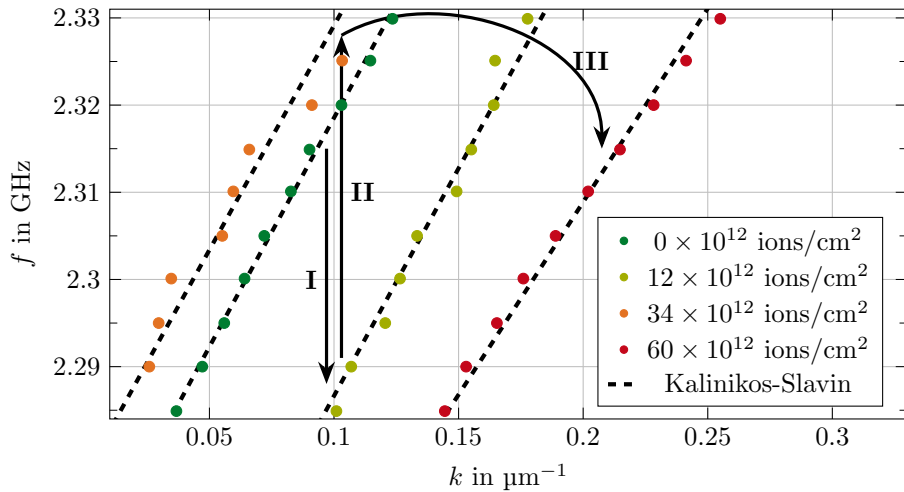


Figure 6: Three prominent spin-wave dispersion shifts across the 30 regions irradiated at 30 keV. (I) The curve shifts to lower frequencies for implantation doses up to 12×10^{12} ions/cm 2 . (II) For doses increasing up to 34×10^{12} ions/cm 2 , the curve shifts back to higher frequencies. (III) At doses of 60×10^{12} ions/cm 2 and above, the curve again shifts to lower frequencies and exhibits an additional change in slope.

The dose-dependent t_{eff} is determined from AFM height measurements performed after wet-chemical etching, as shown in Fig. 7(a). In addition to the uniform etching offset $\Delta t_0 = 4.09$ nm, irradiated regions exhibit a dose- and energy-dependent height reduction Δt_{FIB} , reflecting preferential removal of amorphized material. This thickness reduction is incorporated into the dispersion analysis by $t_{\text{eff}} = 100$ nm $- \Delta t_0 - \Delta t_{\text{FIB}}$.

The trMOKE-derived dispersion data for all irradiated squares at 30 keV are fitted using Eq. (7), with their corresponding t_{eff} . This analysis reveals systematic, dose-dependent modifications of the spin-wave dispersion. Representative dispersion curves illustrating this evolution are shown in Fig. 6. At low irradiation doses, the dispersion shifts monotonically toward lower frequencies, reflecting a progressive decrease of H_{mel} associated with strain accumulation (phase I). At intermediate doses, the dispersion trend reverses and shifts toward higher frequencies, indicating a partial relaxation of the local strain due to irradiation-induced dislocation motion (phase II). Upon further increasing the dose, the dispersion shifts downward once more

and approaches saturation, consistent with renewed strain buildup combined with near-surface amorphization Δt_{FIB} (phase III).

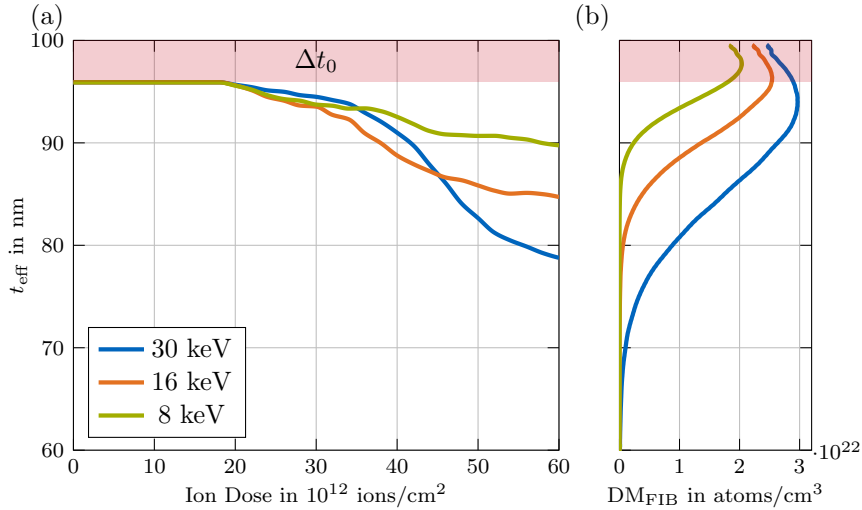


Figure 7: Height profiles of the effective film thickness t_{eff} and simulated damage model DM_{FIB} . (a) AFM height profiles of regions implanted with different ion doses after a 120 s wet-chemical etching step (etching offset Δt_0), shown for three acceleration voltages. (b) For the highest dose, $60 \cdot 10^{12}$ ions/cm 2 , the corresponding DM_{FIB} distribution is displayed, enabling comparison between the measured thickness variations and the simulated ion penetration depth.

Complementary SRIM Monte Carlo simulations are employed to determine the depth distribution of irradiation-induced damage. As shown in Fig. 7(b), the experimentally observed saturation of the irradiation-induced thickness reduction Δt_{FIB} occurs at depths that are in good agreement with the simulated ion penetration range, hereafter denoted as $\Delta t_{\text{FIB},\text{max}}$. This close correspondence between experiment and simulation suggests that the SRIM simulations provide a reliable approximation of the actual damage profile within the YIG film, consistent with [16, 26]. Consequently, we assume that the simulated damage distribution can be directly related to the spatial distribution of irradiation-induced deformations and, therefore, to the three-phase scenario. In the following section, this assumption forms the basis for the development of a qualitative, SRIM-based three-phase scenario describing the depth-dependent deformation across the three identified phases.

3.4 SRIM-Based Modelling of the Three-Phase Scenario

To interpret the observed dispersion shifts within the framework of the three-phase scenario at a fundamental level, a structural model is required that captures the development of irradiation-induced strain within the crystal. This model provides the physical basis for attributing the fitted dispersion changes to magnetoelastic effects, thereby justifying the extraction of H_{mel} from the dispersion analysis (Fig. 6). We therefore introduce a qualitative strain model that describes the accumulation, relaxation, and partial breakdown of lattice strain as a function of increasing Ga^+ ion dose.

Motivated by the three-phase scenario, the SRIM-based three-phase scenario focuses on the depth-dependent distribution of irradiation-induced damage and the associated onset of dislocation nucleation, as introduced in Sec. 3.2. This distribution is quantified using SRIM simulations. The calculated damage models, denoted DM_{FIB} , form the basis of the strain description and enable the construction of the qualitative strain profile shown in Fig. 8 (blue solid line). In this representation, the calculated damage is mapped onto a depth-dependent relative strain profile $\bar{\varepsilon}(d)$.

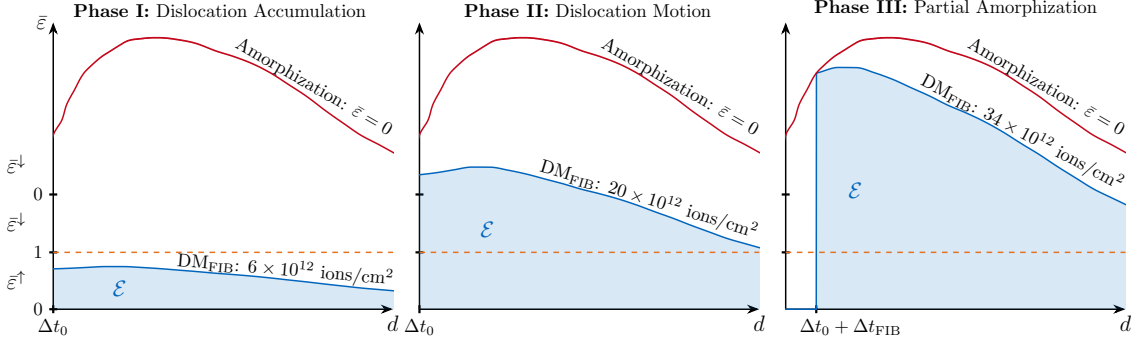


Figure 8: Qualitative strain model at 30 keV illustrating the three deformation regimes Phase I: Dislocation Accumulation, Phase II: Dislocation Motion, and Phase III: Partial Amorphization. The relative strain $\bar{\varepsilon}(d)$ is shown as a function of depth d for normalized damage models DM_{FIB} at ion doses of 6×10^{12} ions/cm 2 , 20×10^{12} ions/cm 2 , and 34×10^{12} ions/cm 2 . The dashed orange line denotes the phase I-II threshold $DM_{I,II}$, and the solid red line the depth-dependent amorphization boundary $DM_{II,III}$, beyond which $\bar{\varepsilon} = 0$. The shaded area indicates the summed relative strain \mathcal{E} used to evaluate the mean relative strain $\langle \bar{\varepsilon} \rangle$.

In the SRIM-based three-phase scenario the three deformation phases are delineated by introducing two characteristic damage boundaries. The first boundary (dashed orange line) marks the end of source hardening, where increasing damage leads to continued strain accumulation, denoted $\bar{\varepsilon}^\uparrow$. Beyond this boundary, plastic deformation becomes active and strain relaxation sets in, corresponding to $\bar{\varepsilon}^\downarrow$. The second boundary (solid red line) marks the relative strain $\bar{\varepsilon}$ at which strain release is exhausted. Above this boundary, the crystal can no longer accommodate dislocations and transitions into an amorphous state, for which $\bar{\varepsilon} = 0$ is assumed.

For an acceleration voltage of 30 keV, both phase boundaries are determined phenomenologically. The first boundary is obtained by calculating DM_{FIB} at an ion dose of 8×10^{12} ions/cm 2 . This dose is chosen because the corresponding maximum damage density defines a characteristic strain state. Within the model, this strain state reproduces the qualitative behavior observed experimentally, namely the turning point at approximately 12×10^{12} ions/cm 2 in Fig. 6, where the dispersion curve reverses its trend and shifts upward (II).

Importantly, this turning point does not mark the physical onset of plastic deformation itself. Instead, it corresponds to the dose at which strain relaxation mediated by plastic deformation becomes dominant over further elastic strain accumulation within the framework of the model. Plastic deformation is assumed to already initiate at doses as low as 8×10^{12} ions/cm 2 , where a critical damage density of $DM_{I,II} = 3.97 \times 10^{21}$ atoms/cm 3 is reached. As a result, the transition between phase I and phase II represents a mixed regime in which only the most highly strained depths of the crystal undergo plastic deformation, while other depths remain in phase I and continue to accumulate strain, consistent with the bell-shaped depth profile of DM_{FIB} .

A similar strategy is employed to determine the amorphization threshold. In this case, the second boundary (solid red line in Fig. 8) is obtained in an inverse manner by identifying the depth-dependent damage densities required to reproduce the AFM-measured effective thickness t_{eff} shown in Fig. 7(a) (blue line). This boundary does not correspond to a single, sharply defined damage density value. Instead, it follows the discrete damage densities necessary to reproduce the measured thickness reduction, starting from $d = \Delta t_0$ and extending to the dose-dependent depth $d = \Delta t_0 + \Delta t_{FIB}$, where Δt_{FIB} increases with ion dose. This procedure results in the bent boundary observed in Fig. 8, which we denote as $DM_{II,III}$.

Since the strain distribution within the crystal is not defined explicitly, we introduce a relative strain metric based on the damage models introduced above. At each depth position d , the local strain is defined relative to the phase I-II damage threshold $DM_{I,II}$. To this end, we introduce

the normalized damage variables

$$x(d) := \frac{DM_{FIB}(d)}{DM_{I,II}}, \quad x_{II,III}(d) := \frac{DM_{II,III}(d)}{DM_{I,II}}, \quad (8)$$

from which the relative strain metric is defined as

$$\bar{\varepsilon}(d) = \begin{cases} x(d), & x(d) < 1, \\ 2 - x(d), & 1 \leq x(d) < x_{II,III}(d), \\ 0, & x(d) \geq x_{II,III}(d). \end{cases} \quad (9)$$

This piecewise definition directly maps the local damage state onto the three deformation regimes and captures both the buildup and subsequent release of strain throughout the crystal depth. Moreover, it enforces vanishing strain at depth positions where the local damage exceeds the depth-dependent amorphization boundary $x_{II,III}(d)$, thereby defining the strain metric in our SRIM-based three-phase scenario. The mean relative strain is therefore evaluated only over those depth positions that remain crystalline,

$$\langle \bar{\varepsilon} \rangle = \frac{1}{n} \mathcal{E}, \quad \mathcal{E} := \sum_{i=1}^n \bar{\varepsilon}(d_i), \quad (10)$$

where the averaging is restricted to depth positions $d_i > \Delta t_0 + \Delta t_{FIB}$.

The evolution of $\bar{\varepsilon}(d)$ with increasing ion dose is shown in Fig. 8 as blue solid lines. For each dose, DM_{FIB} is obtained by multiplying the simulated SRIM damage profile by the corresponding ion dose and normalizing it according to Eq. (8). The damage profiles are exemplarily calculated for ion doses of 6×10^{12} ions/cm², 20×10^{12} ions/cm², and 34×10^{12} ions/cm², illustrating the progressive increase of $x(d)$ with dose.

At low ion doses, where $x(d) < 1$ throughout the crystalline depth, the relative strain follows $\bar{\varepsilon}(d) = x(d)$ and increases continuously with increasing damage. This regime corresponds to elastic deformation, in which the linear stress-strain response is reflected by the linear increase of $x(d)$ with ion dose. According to the three-phase scenario, dislocations accumulate within the strain-potential well, leading to the continuous strain buildup characteristic of source hardening.

Once the local damage exceeds $DM_{I,II}$, such that $x(d) > 1$ at specific depth positions, the strain metric enters the second branch of Eq. (9). This defines phase II, in which $\bar{\varepsilon}(d) = 2 - x(d)$ decreases with increasing damage, reflecting strain release via plastic deformation. Because $x(d)$ is bounded not only by unity but also by the depth-dependent amorphization threshold $x_{II,III}(d)$, negative values of $\bar{\varepsilon}$ can be attained when $x_{II,III}(d) > 2$. In this regime, the metric allows for strain states below the initial reference level, which can be interpreted as an improvement of crystalline order compared to the as-fabricated or as-annealed material.

This strain relaxation behavior is not strictly linear, as it is governed by nonlinear plastic deformation associated with dislocation motion. Such nonlinearity cannot be captured by a linearly increasing DM_{FIB} alone, but is instead partially encoded in the non-uniform shape of the depth-dependent amorphization boundary $x_{II,III}(d)$. The bending of this boundary, shown in Fig. 8, constrains the number of dislocations that can be released into neighboring strain-potential wells at a given depth d . As a consequence, these wells fill successively starting from obstacles such as the sample surface. The associated pile-up of dislocations at these obstacles is not explicitly incorporated in the model, which therefore neglects friction hardening and the resulting gradual reaccumulation of strain once further release into adjacent wells is no longer possible. Instead, the model assumes direct partial amorphization following dislocation release, initiating at the surface. Furthermore, a more comprehensive treatment, for example through the introduction of a depth-dependent $DM_{I,II}$, would require explicit modeling of dislocation dynamics and is therefore beyond the scope of this work.

At sufficiently high damage levels, where $x(d) \geq x_{\text{II,III}}(d)$, the corresponding depth positions transition into the amorphous state, and the local relative strain is set to $\bar{\varepsilon}(d) = 0$. These amorphized depths are no longer considered part of the active crystal, and the mean relative strain $\langle \bar{\varepsilon} \rangle$ is evaluated only over the remaining crystalline thickness t_{eff} . Deeper layers may still exhibit elastic or plastic behavior depending on their local value of $\bar{\varepsilon}(d)$, while the crystal at $d = \Delta t_0 + \Delta t_{\text{FIB}}$ progressively becomes amorphous.

3.5 Justification of the Magnetoelastic Interpretation of the Three-Phase Scenario

Using H_{mel} in Eq. (2) as the sole fitting parameter in Eq. (7), we analyze the dispersion shifts discussed in Sec. 3.3. The resulting dose-dependent trend for an ion beam accelerated to 30 keV is shown as the solid line in Fig. 9. Two distinct turning points appear at 12×10^{12} ions/cm² and 34×10^{12} ions/cm², followed by a saturation plateau at about 50×10^{12} ions/cm².

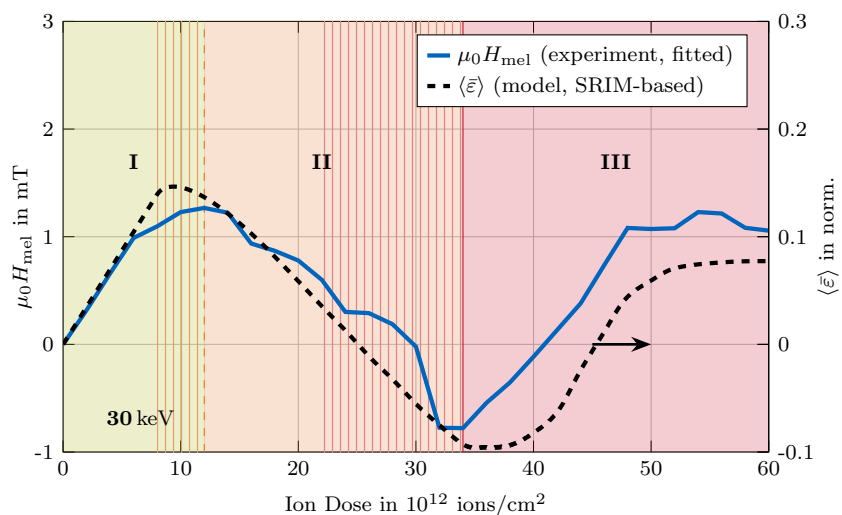


Figure 9: Magnetoelastic field variation $\mu_0 H_{\text{mel}}$ (solid line), extracted from fitting the Kalinikos–Slavin model, as a function of implantation dose. The experimental trend is compared with the simulated mean relative strain $\langle \bar{\varepsilon} \rangle$ (dashed line) modeled by the SRIM-based three-phase scenario at 30 keV. Both curves exhibit the same characteristic turning points and saturation plateau, reflecting the progression through phases I–III and their corresponding intermediate regimes.

A direct comparison using a fixed scaling ($1 \text{ mT} \approx 0.1$) between the strain reflected by $\mu_0 H_{\text{mel}}$ (Fig. 9, solid line) and the simulated $\langle \bar{\varepsilon} \rangle$ (Fig. 9, dashed line) reveals a close correspondence between the two quantities. In particular, both curves exhibit the same characteristic turning points and converge to an identical saturation plateau. These signatures correspond directly to phases I–III but also to intermediate regimes in which multiple phases coexist across different material depths. In these intermediate regimes (highlighted by the striped areas in Fig. 9), individual layers may already enter phase II or phase III, while the overall crystalline structure is still dominated by the preceding phase. The turning points therefore mark the ion doses at which the dominant contribution to the overall strain shifts from phase I to phase II, and later from phase II to phase III. Within the assumptions of the modeled scenario, this parallel evolution supports the interpretation that the two turning points in the dose-dependent spin-wave wavelength observed in Fig. 2(b) arise from successive transitions between elastic strain accumulation, plastic strain relaxation, and partial amorphization. The observed agreement supports the plausibility of the proposed three-phase scenario and the corresponding magnetoelectric treatment of ion-induced strain for the 30 keV, without constituting direct evidence of the

underlying microscopic mechanisms.

Using the same phenomenological determination of the phase boundaries as established for 30 keV in Sec. 3.4, we extend our analysis to lower ion-beam acceleration voltages of 16 keV and 8 keV, as shown in Fig. 10, in order to further assess the robustness of the modeling. The extracted magnetoelastic field $\mu_0 H_{\text{mel}}$ exhibits a consistent magnitude across all acceleration voltages. In contrast, the strain values $\langle \bar{\varepsilon} \rangle$ derived from both modeled SRIM-based three-phase scenarios, evaluated using the same fixed scaling for comparison, decrease systematically with decreasing ion acceleration. This results in increasing quantitative deviations between experiment and model, which are most pronounced at 8 keV (Fig. 10(b)).

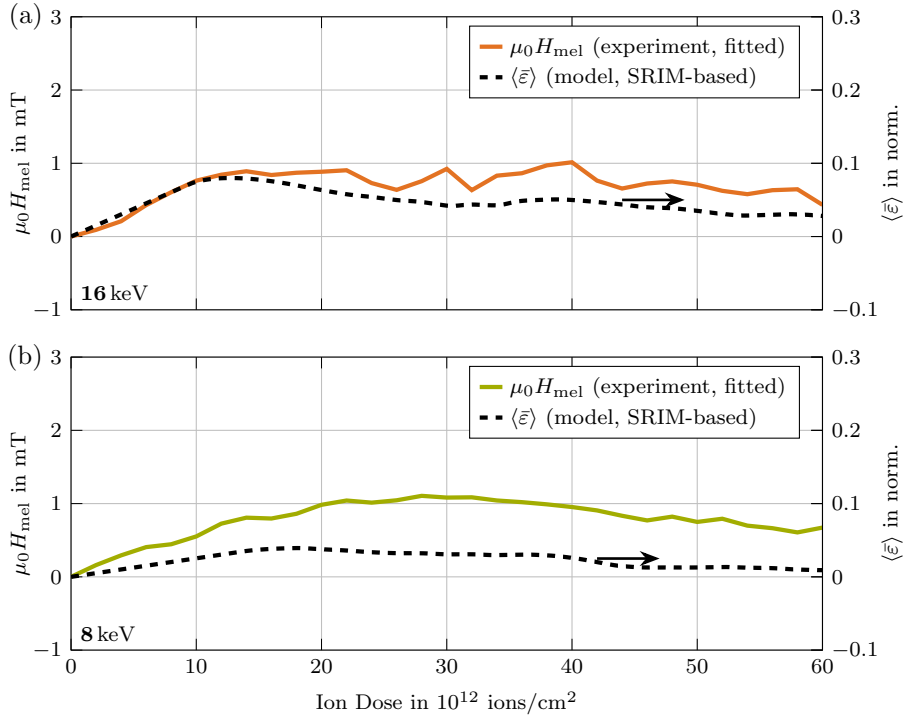


Figure 10: Magnetoelastic field variation $\mu_0 H_{\text{mel}}$ (solid lines), extracted from fitting the Kalinikos–Slavin model, shown as a function of ion implantation dose. The experimental results are compared to the simulated mean relative strain $\langle \bar{\varepsilon} \rangle$ (dashed lines) modeled by the SRIM-based three-phase scenario, using the phase-boundary calibration established at 30 keV, for acceleration voltages of (a) 16 keV and (b) 8 keV.

These deviations are primarily attributed to the limited information available on the prestrained state of the film after annealing and its depth distribution prior to irradiation. In the present approach, information on the prestrained state is inferred indirectly via the inverse determination of the amorphization boundary using the etch-induced thickness reduction Δt_{FIB} , which corresponds to the irradiation-induced thickness change. The maximum thickness reduction $\Delta t_{\text{FIB},\text{max}}$ reflects the maximum penetration depth of the ion beam at a given acceleration voltage. At lower acceleration voltages, the reduced penetration depth and the associated damage cascade result in a smaller $\Delta t_{\text{FIB},\text{max}}$, thereby limiting the depth range over which the prestrained state of the film can be effectively reconstructed. Consequently, the relative strain profile $\bar{\varepsilon}(d)$ is averaged over an effective thickness t_{eff} , while assuming $\bar{\varepsilon}(d) = 0$ for $d > \Delta t_0 + \Delta t_{\text{FIB},\text{max}}$. This assumption artificially lowers the mean relative strain $\langle \bar{\varepsilon} \rangle$, even though $\bar{\varepsilon}(d) \neq 0$ may persist beyond $d > \Delta t_0 + \Delta t_{\text{FIB},\text{max}}$, where an unknown prestrain is not captured by the model. This reduced depth sensitivity naturally leads to lower apparent $\langle \bar{\varepsilon} \rangle$, owing to the increased contribution of depths where $\bar{\varepsilon} = 0$ in the averaging procedure. This effect, in turn, contributes to the observed quantitative deviations at lower ion accelerations. A

more accurate quantitative comparison would therefore require a depth-resolved strain profile of the pristine film prior to irradiation. Nevertheless, despite these quantitative deviations in the absolute magnitude, the overall shape of the strain profile is consistently reproduced across all acceleration voltages.

To complete our investigation, we employ micromagnetic simulations to numerically reproduce the experimentally observed wavelength shifts. These simulations do not constitute an independent model for the dispersion evolution. Instead, they serve as a consistency check, demonstrating that the effective strain states inferred from the dispersion analysis and the SRIM-based three-phase scenario are sufficient to reproduce the measured spin-wave behavior within a full magnetoelastic micromagnetic framework. Importantly, all strain-related input parameters used in the simulations are fully determined by the experimentally extracted magnetoelastic field or by the simulated strain model. For this purpose, we examined the strain-tensor components in Eq. (1) and their contribution to the magnetoelastic field \mathbf{H}_{mel} in Eq. (3). Since the actual strain tensor inside the irradiated crystal is unknown, and our dispersion analysis provides only an effective expression for \mathbf{H}_{mel} in an OOP configuration, further simplifications are required. We therefore assume a small uniaxial deformation in a homogeneous cubic crystal, allowing the strain tensor to be simplified using classical elasticity theory [27]. Under this assumption, Hooke's law in three dimensions reduces to

$$\boldsymbol{\varepsilon} = \begin{bmatrix} \varepsilon_{xx} & 0 & 0 \\ 0 & \varepsilon_{yy} & 0 \\ 0 & 0 & \varepsilon_{zz} \end{bmatrix} = \begin{bmatrix} -\nu\varepsilon_{zz} & 0 & 0 \\ 0 & -\nu\varepsilon_{zz} & 0 \\ 0 & 0 & \varepsilon_{zz} \end{bmatrix}, \quad (11)$$

where a uniaxial strain in the z -direction produces transverse strains via the Poisson effect.

Since Eq. (11) does not include shear components, Eq. (3) simplifies to

$$H_{\text{mel}} = -\frac{2}{\mu_0 M_s} B_1 \varepsilon_{zz}. \quad (12)$$

which allows us to directly convert the experimentally extracted values of H_{mel} into the corresponding out-of-plane strain component ε_{zz} . For the experimental data, the resulting ε_{zz} values are subsequently inserted into Eq. (11) to determine the transverse strain components ε_{xx} and ε_{yy} via the Poisson effect. By contrast, within the SRIM-based three-phase scenario, the simulated $\langle \bar{\varepsilon} \rangle$ is directly mapped onto H_{mel} using the scaling shown in Fig. 9 and Fig. 10. The full strain tensor $\boldsymbol{\varepsilon}$ is then constructed analogously using Eq. (11).

Using $B_1 = 3.48 \times 10^5$ J/m³, $M_s = 130$ kA/m, and a Poisson ratio of $\nu = 0.29$, we obtain the complete strain tensor $\boldsymbol{\varepsilon}$ for all ion doses. Both the experimentally extracted strain values and those obtained from the SRIM-based three-phase scenario modeled at 30 keV already incorporate the effective outcome of the nonlinear lattice response associated with plastic deformation, as encoded in H_{mel} and $\langle \bar{\varepsilon} \rangle$. Consequently, no additional shear- or plasticity-specific strain components need to be introduced. The resulting strain tensors can therefore be inserted directly into micromagnetic simulations, enabling a quantitative replication of the experimentally observed dose-dependent wavelength shifts shown in Fig. 2.

Figure 11 compares the experimentally extracted wavelengths with micromagnetic simulations performed using two different strain inputs: strain-tensor components calculated directly from the experimentally fitted H_{mel} , and $\langle \bar{\varepsilon} \rangle$ derived from the SRIM-based three-phase scenario modeled at 30 keV. Despite the simplifying assumptions, the strain tensors employed in the simulations reproduce the overall wavelength evolution reasonably well, apart from isolated outliers around 32×10^{12} ions/cm².

The observed outliers originate from regimes in which spin-wave excitation becomes increasingly inefficient, for instance when the excitation is beyond FMR or when the resulting wavelengths approach or exceed the finite simulation window.

Besides these physical excitation limits and the numerical constraints imposed by the finite simulation window, quantitative deviations can also arise from simplifications inherent in

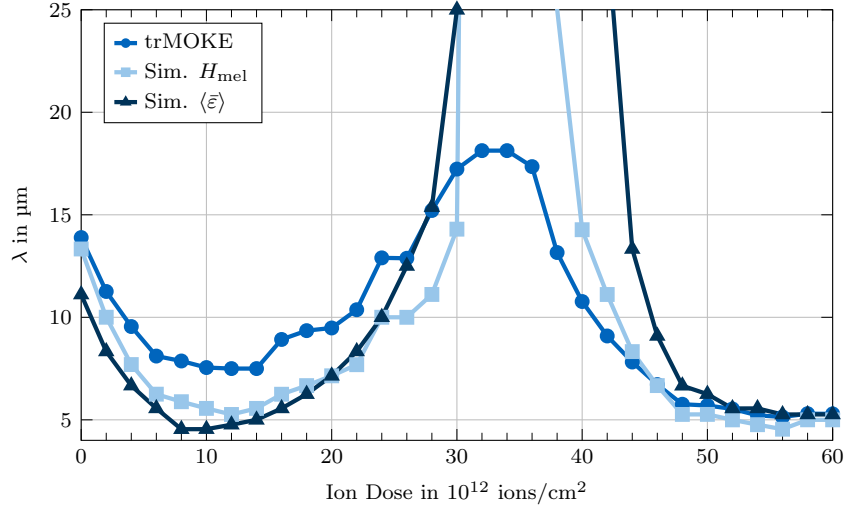


Figure 11: Comparison of wavelength shifts as a function of ion dose, extracted from line-wise Fourier transformations of the measured spin-wave profiles at 2.305 GHz and 8 dBm under an external field of $\mu_0 H_{\text{ext}} = 250$ mT. The experimental data (trMOKE) are compared with micromagnetic simulations using two different strain inputs: strain-tensor components derived from the experimentally fitted magnetoelastic field H_{mel} , and the mean relative strain $\langle \bar{\varepsilon} \rangle$ obtained from the SRIM-based three-phase scenario modeled at 30 keV.

Eq. (11) or in the dispersion fitting procedure. In particular, the fit assumes a constant effective magnetization M_{eff} . In the dispersion fitting procedure, the M_{eff} and H_{mel} enter the Kalinikos–Slavin formalism in a correlated manner. Variations in H_{mel} can therefore be partially compensated by corresponding changes in M_{eff} , leading to non-unique parameter combinations that reproduce the measured dispersion equally well. Allowing both parameters to vary simultaneously would require additional independent constraints, which are not available from the present data set. To avoid this ambiguity, M_{eff} was kept fixed, and all dose-dependent changes in the dispersion were attributed to variations in H_{mel} . While this choice can introduce systematic deviations in the extracted values, it ensures a well-defined and physically interpretable fitting procedure.

Owing to the additional simplifications and assumptions inherent to the SRIM-based three-phase scenario, the quantitative deviations are further increased for the strain tensors derived from this approach, resulting in a poorer agreement with the trMOKE data compared to the strain values obtained from the experimentally fitted H_{mel} .

4 Discussion

Despite the simplifications inherent in the analysis, the results provide consistent evidence that FIB-steered spin-wave propagation originates from magnetoelastic effects. The observed turning points in the spin-wave wavelength with increasing ion dose directly correlate with the evolution of a strain-induced magnetoelastic field, accompanied at higher doses by an effective thickness reduction due to partial amorphization of the magnetic layer.

The experimental findings are well described by a three-phase deformation scenario of crystalline YIG under Ga^+ irradiation. This interpretation is supported by a simplified SRIM-based three-phase scenario that captures the dose-dependent damage profile and its correspondence to the three deformation regimes and the observed magnetoelastic behavior. Micromagnetic simulations further corroborate this picture, showing that the combined effects of strain-induced fields and thickness reduction reproduce the measured spin-wave steering.

The distinction between elastic and plastic deformation regimes suggests clear directions for future work. In particular, limiting irradiation to the elastic regime may enable post-annealing recovery, opening pathways toward reversible or reconfigurable strain-based spin-wave control.

In summary, this study establishes magnetoelastic coupling as a practical and quantitatively relevant mechanism for tailoring spin-wave dispersion with focused ion beams, providing a foundation for strain-engineered magnonic devices.

Acknowledgment

This work was funded by the Deutsche Forschungsgemeinschaft (DFG, German Research Foundation) – Project number 514146693. We further acknowledge the sponsoring support of “Make ideas real. Rohde & Schwarz @ ZEITlab”, who provided access to the FIB technology.

References

- [1] G. Csaba, A. Papp, and W. Porod. Perspectives of using spin waves for computing and signal processing. *Physics Letters A*, 381(17):1471–1476, 2017.
- [2] A. Mahmoud, F. Ciubotaru, F. Vanderveken, A. V. Chumak, S. Hamdioui, C. Adelmann, and S. Cotofana. Introduction to spin wave computing. *Journal of Applied Physics*, 128(16), 2020.
- [3] G. Csaba, A. Papp, and W. Porod. Spin-wave based realization of optical computing primitives. *Journal of Applied Physics*, 115(17), 2014.
- [4] C. S. Davies and V. V. Kruglyak. Graded-index magnonics. *Low Temperature Physics*, 41(10):760–766, 2015.
- [5] M. Kiechle, A. Papp, S. Mendisch, V. Ahrens, M. Golibrzuch, G. H. Bernstein, W. Porod, G. Csaba, and M. Becherer. Spin-wave optics in yig realized by ion-beam irradiation. *Small*, 19(21):2207293, 2023.
- [6] Q. Wang, A. V. Chumak, and P. Pirro. Inverse-design magnonic devices. *Nature Communications*, 12(1):2636, 2021.
- [7] A. Papp, W. Porod, and G. Csaba. Nanoscale neural network using non-linear spin-wave interference. *Nature Communications*, 12(1):6422, 2021.
- [8] S. Breitkreutz, J. Kiermaier, I. Eichwald, X. Ju, G. Csaba, D. Schmitt-Landsiedel, and M. Becherer. Majority Gate for Nanomagnetic Logic with Perpendicular Magnetic Anisotropy. *IEEE Transactions on Magnetics*, 48(11):4336–4339, 2012.
- [9] M. Becherer, S. Breitkreutz-v. Gamm, I. Eichwald, G. Źiemys, J. Kiermaier, G. Csaba, and D. Schmitt-Landsiedel. A monolithic 3D integrated nanomagnetic co-processing unit. *Solid-State Electronics*, 115, Part B:74–80, 2016.
- [10] V. Ahrens, L. Gnoli, D. Giuliano, S. Mendisch, M. Kiechle, F. Riente, and M. Becherer. Skyrmion velocities in fib irradiated w/cofeb/mgo thin films. *AIP Advances*, 12(3), 2022.
- [11] V. Ahrens, C. Kiesselbach, L. Gnoli, D. Giuliano, S. Mendisch, M. Kiechle, F. Riente, and M. Becherer. Skyrmions under control—fib irradiation as a versatile tool for skyrmion circuits. *Advanced Materials*, 35(2):2207321, 2023.
- [12] J. Bensmann, R. Schmidt, K. O. Nikolaev, D. Raskhodchikov, S. Choudhary, R. Bhardwaj, S. Taheriniya, A. Varri, S. Niehues, A. El Kadri, et al. Dispersion-tunable low-loss implanted spin-wave waveguides for large magnonic networks. *Nature Materials*, pages 1–7, 2025.

- [13] M. Kiechle, L. Maucha, V. Ahrens, C. Dub, W. Porod, G. Csaba, M. Becherer, and A. Papp. Experimental demonstration of a spin-wave lens designed with machine learning. *IEEE Magnetics Letters*, 13:1–5, 2022.
- [14] J. Greil, M. Kiechle, A. Papp, P. Neumann, Z. Kovács, J. Volk, F. Schulz, S. Wintz, M. Weigand, G. Csaba, et al. The effect of ga-ion irradiation on sub-micron-wavelength spin waves in yttrium-iron-garnet films. *Nanotechnology*, 36(13):135301, 2025.
- [15] J. Mada and K. Asama. Fmr study of an ion-implanted layer on bubble garnet films. *Journal of Applied Physics*, 50(9):5914–5919, 1979.
- [16] I. Fodchuk, A. Kotsyubynsky, A. Velychkovych, I. Hutsuliak, V. Boychuk, V. Kotsyubynsky, and L. Ropyak. The effect of ne^+ ion implantation on the crystal, magnetic, and domain structures of yttrium iron garnet films. *Crystals*, 12(10):1485, 2022.
- [17] G. S. Was. *Fundamentals of Radiation Materials Science: Metals and Alloys*. Springer, 2007.
- [18] B. A. Kalinikos and A. N. Slavin. Theory of dipole-exchange spin wave spectrum for ferromagnetic films with mixed exchange boundary conditions. *Journal of Physics C: Solid State Physics*, 19(35):7013, 1986.
- [19] J. F. Ziegler, M. D. Ziegler, and J. P. Biersack. Srim—the stopping and range of ions in matter (2010). *Nuclear Instruments and Methods in Physics Research Section B*, 268(11–12):1818–1823, 2010.
- [20] A. Vansteenkiste, J. Leliaert, M. Dvornik, M. Helsen, F. Garcia-Sanchez, and B. Van Waeyenberge. The design and verification of mumax3. *AIP Advances*, 4(10), 2014.
- [21] S. B. Ubizskii, A. O. Matkovskii, N. Mironova-Ulmane, V. Skvortsova, A. Suchocki, Y. A. Zhydachevskii, and P. Potera. Displacement defect formation in complex oxide crystals under irradiation. *Physica Status Solidi (a)*, 177(2):349–366, 2000.
- [22] A. B. Smith and R. V. Jones. Magnetostriction constants from ferromagnetic resonance. *Journal of Applied Physics*, 34(4):1283–1284, 1963.
- [23] B. Bhoi, B. Kim, Y. Kim, M. Kim, J. Lee, and S. Kim. Stress-induced magnetic properties of pld-grown high-quality ultrathin yig films. *Journal of Applied Physics*, 123(20), 2018.
- [24] P. M. Anderson, J. P. Hirth, and J. Lothe. *Theory of Dislocations*. Cambridge University Press, 2017.
- [25] F. Vanderveken, J. Mulders, J. Leliaert, B. Van Waeyenberge, B. Soree, O. Zografos, F. Ciubotaru, and C. Adelmann. Finite difference magnetoelastic simulator. *Open Research Europe*, 1:35, 2021.
- [26] K. Höflich, G. Hobler, F. I. Allen, T. Wirtz, G. Rius, L. McElwee-White, A. V. Krasheninnikov, M. Schmidt, I. Utke, N. Klingner, et al. Roadmap for focused ion beam technologies. *Applied Physics Reviews*, 10(4), 2023.
- [27] L. D. Landau, L. P. Pitaevskii, A. M. Kosevich, and E. M. Lifshitz. *Theory of Elasticity*, volume 7. Elsevier, 2012.